8.1 INFLUENCE OF AMBIENT ENVIRONMENTAL CONDITIONS AND OROGRAPHY ON THE CHARACTERISTICS OF DEEP CONVECTIVE CELLS AS SIMULATED WITH A SOPHISTICATED TWO-MOMENT (BULK) MICROPHYSICAL SCHEME

Ulrich Blahak*, H. Noppel and Klaus D. Beheng
Institut für Meteorologie und Klimaforschung, Universität Karlsruhe / Forschungszentrum Karlsruhe

1 INTRODUCTION

The influence of orography and ambient environmental conditions (aerosol conditions, profiles of temperature, humidity and wind) on the initiation, life cycle and precipitation efficiency of convective cells is a current topic in meteorological research as well as in numerical weather prediction.

In order to elaborate parameters crucially affecting the development of convective cells high resolution cloud resolving 3D simulations ($\Delta x \leq 1$ km) with a test version of the operational nonhydrostatic Lokalmodell (LM) of the German Weather Service are performed. In contrast to other studies, we use a sophisticated cloud microphysics parameterization, the two-moment bulk microphysical scheme by Seifert and Beheng (2006). In this way, the complex microphysical/(thermo)dynamical feedback processes in clouds are quite accurately described while keeping the numerical costs affordable for full 3D simulations.

In detail, idealized high resolution cloud resolving simulations are performed considering simplified orography (e.g., elongated mountain ridge). As influencing parameters, temperature- and humidity profiles, condensation- and 0°C-level and maritime/continental CCN conditions are varied as well as mountain width and height to investigate the combined effects of different (thermo)dynamic conditions and orographic flow modification on single convective systems. The ultimate goal is to find parameters allowing to discriminate different convective regimes, useful for convection parameterizations and for nowcasting purposes.

In a first stage, certain processes and sensitivities are identified and investigated in a more or less ”spot check” fashion. This paper presents examples of these investigations. To switch over to a more systematic process- and parameter study, the next step will be to identify the most prominent sensitivities and to choose a suitable subset (no more than approx. 3 or 4 parameters) for a detailed sensitivity study to keep the computational effort within manageable limits.

In parallel, radar reflectivity measurements of single deep convective systems are compared to accompanying model simulated reflectivities to check the model setup and results in a qualitative way.

In Chapter 2 the model setup is briefly described, Chapter 3 shows an example of comparison with radar data, and in Chapters 4 and 5 two examples of interesting sensitivities are presented.

**Corresponding author address:* Ulrich Blahak, Institut für Meteorologie und Klimaforschung, Universität Karlsruhe / Forschungszentrum Karlsruhe, Postfach 3640, D-76021 Karlsruhe, Germany;
e-mail: ulrich.blahak@imk.fzk.de.

Tab. 1: Settings and parameters used for the LM runs:

Horiz. resolution	1 km
Vert. resolution	40 m – 600 m (64 layers)
Operator splitting	Marchuk
Time splitting	Klemp-Wilhelmson (slow modes/ sound wave modes)
Large timestep	6 s
Time discretisation	3rd order Runge-Kutta
Advection of dyn. variables	Upwind 5th order
Advection of positive definite moisture quantities	Bott-2
Initial conditions	Idealized, horiz. homogeneous
Boundary conditions	Lateral: fixed Upper: Sponge layer Lower: free- or no-slip
Turbulence param.	TKE-based, 3-D, including ”moist” effects
Soil- and vegetation model	off
Radiation model	off
Convection param.	Deep conv.: off Shallow conv.: off

2 MODEL SETUP

The LM is a nonhydrostatic, fully compressible mesoscale weather prediction model. The basic set of equations and numerical techniques are described in detail in Doms and Schättler (2002), and the physical parameterizations are outlined in Doms et al. (2005). Important settings and parameters for our simulations can be found in Table 1.

In its operational version, the LM only includes a relatively simple and efficient five-class one-moment bulk microphysical parameterization scheme. To improve the physical description for our relatively high resolution of $\Delta x = 1$ km, the two-moment bulk microphysical scheme by Seifert and Beheng (2006) has been coupled to the LM. This scheme distinguishes six hydrometeor categories (cloud drops, cloud ice, rain, snow and two graupel classes) and represents each particle type by its respective number and mass density. It also allows the initial cloud droplet size distribution (determined by two moments) to represent either continental or maritime CCN conditions. Note that the second graupel class, exhibiting higher particle bulk density and fall velocity than the original single graupel category, was recently added to the scheme. Now graupel particles initiated by freezing of raindrops (FRI-graupel) and by riming of snow- or cloud ice particles (RIME-graupel) are distinguished, see separate abstract P2.6 by Noppel et al. (2006).

A recent comparison of the two-moment bulk scheme with a spectral (bin) microphysical model (without the additional second graupel class) can be found in Seifert et al. (2006).

As initial and boundary conditions for the idealized simulations essentially the analytic profiles used by Weisman and Klemp (1982) are utilized, but with slight modifications of the temperature level (height of 0-°C-isotherm) and the moisture profile, according to the needs of the sensitivity study under consideration.

3 SOME VERIFICATION BY MEASURED RADAR DATA

Measured radar reflectivity data provide one possibility to check the model system qualitatively by comparing the spatial and temporal evolution of the modeled and measured reflectivity fields. To this end, semi-idealized simulations are performed with the LM and compared to reflectivity measurements obtained by our institution's conventional C-Band Doppler radar. One example is a cell-splitting event which was observed on July 26th 2001 near the city of Mannheim (Germany) in the upper Rhine valley. The right column of Fig. 2 shows, from top to bottom, a sequence of MAX-CAPPI reflectivity images (maximum projections of 3D radar data along horizontal and vertical columns) with a time increment of 20 min. The radar is located at position (0,0). The first image corresponds to 17:20 LT, approx. 15 min after the first echoes were detected. Note that some other convective cells were observed in the radar area at that time, but are omitted in the images for clarity.

July 26th 2001 presented a typical convective weather situation with intense insolation and weak large scale forcing. Ambient thermodynamic conditions were reconstructed from nearby operational radiosonde soundings (Stuttgart, approx. 80 km to the southeast; Nancy, approx. 80 km to the southwest) and measurements of temperature, humidity and windspeed at ground, taken at the radar location. Fig. 1 shows the synthesized temperature-, humidity- and windprofile for the time of the radar observations. The temperature- and dewpoint stratification (red and green line, resp.) is characterized by moist instability up to the tropopause and no significant inversion above the well-mixed boundary layer (ground level up to about 890 hPa). The $CAPE$, corresponding to a parcel with temperature and humidity averaged over the lowest 100 hPa-layer, is about 1700 $\mathrm{J\,kg^{-1}}$. The windspeed below 500 hPa is generally lower than 10 $\mathrm{m\,s^{-1}}$, but the wind direction is significantly changing from northwest below 900 hPa over northeast to southwest above 800 hPa.

First, the radar data show a strong reflectivity core

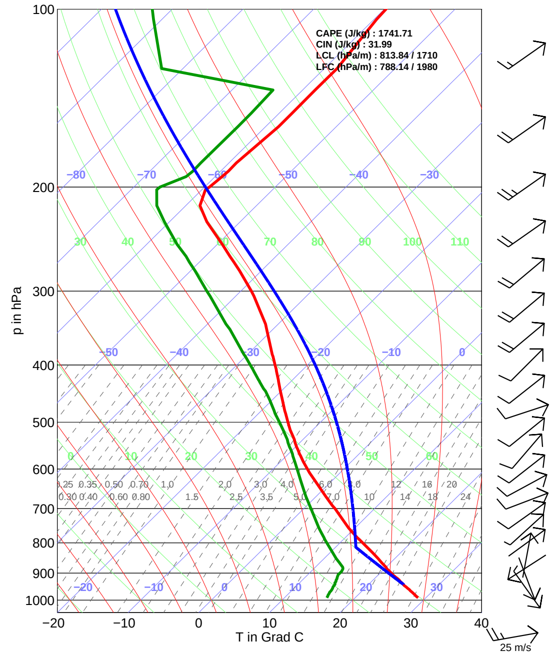

Fig. 1: Log-p/Skew-T diagram of the (supposed) ambient (thermo-)dynamic conditions on July 26th 2001 at about 17:00 LT in the upper Rhine valley. The wind profile is shown by windbarbs to the right of the diagram (short barb = 5 $\mathrm{m\,s^{-1}}$, long barb = 10 $\mathrm{m\,s^{-1}}$).

up to an altitude of 12 km, moving to the northeast. 20 min later, two new cores appear at its left and right flanks, leading to a characteristic "T-shaped" reflectivity structure in the vertical maximum projection. Later, the initial core weakens and the two flanking cores form a pair of split cells. Lateron, the split cells exhibit diverging pathways around a general northeastern direction (not shown here) and dissolve after about 3 h, the lifetime of the rightmoving cell being slightly longer.

The left column of Fig. 2 presents the corresponding reflectivity fields which are derived from hydrometeor number- and mass densities of an accompagnying semi-idealized LM simulation. Maritime CCN conditions are assumed in this case, see Chapter 4 for explanation. No orography is considered here, the initial and time-independent boundary conditions are prescribed according to Fig. 1 and convection is artificially triggered by a "warm bubble" having a diameter of 20 km and excess temperature of 2.5 K. Due to the presumably unrealistic triggering mechanism, one should not interpret the initial cell development stage (about 15 min from triggering, not shown here) but the lateron measured and simulated systems. They show a qualitatively similar development with the characteristic "T-shaped" reflectivity structure. However, the separation of the two splitting cores is somewhat slower and weaker in the model and the model-derived reflectivities at higher altitudes are lower than observed. Note that the reasons for reflectivity differences can be manifold. On one hand, the calculation of reflectivity strongly depends on assumptions on the bulk density and the

Model | Radar

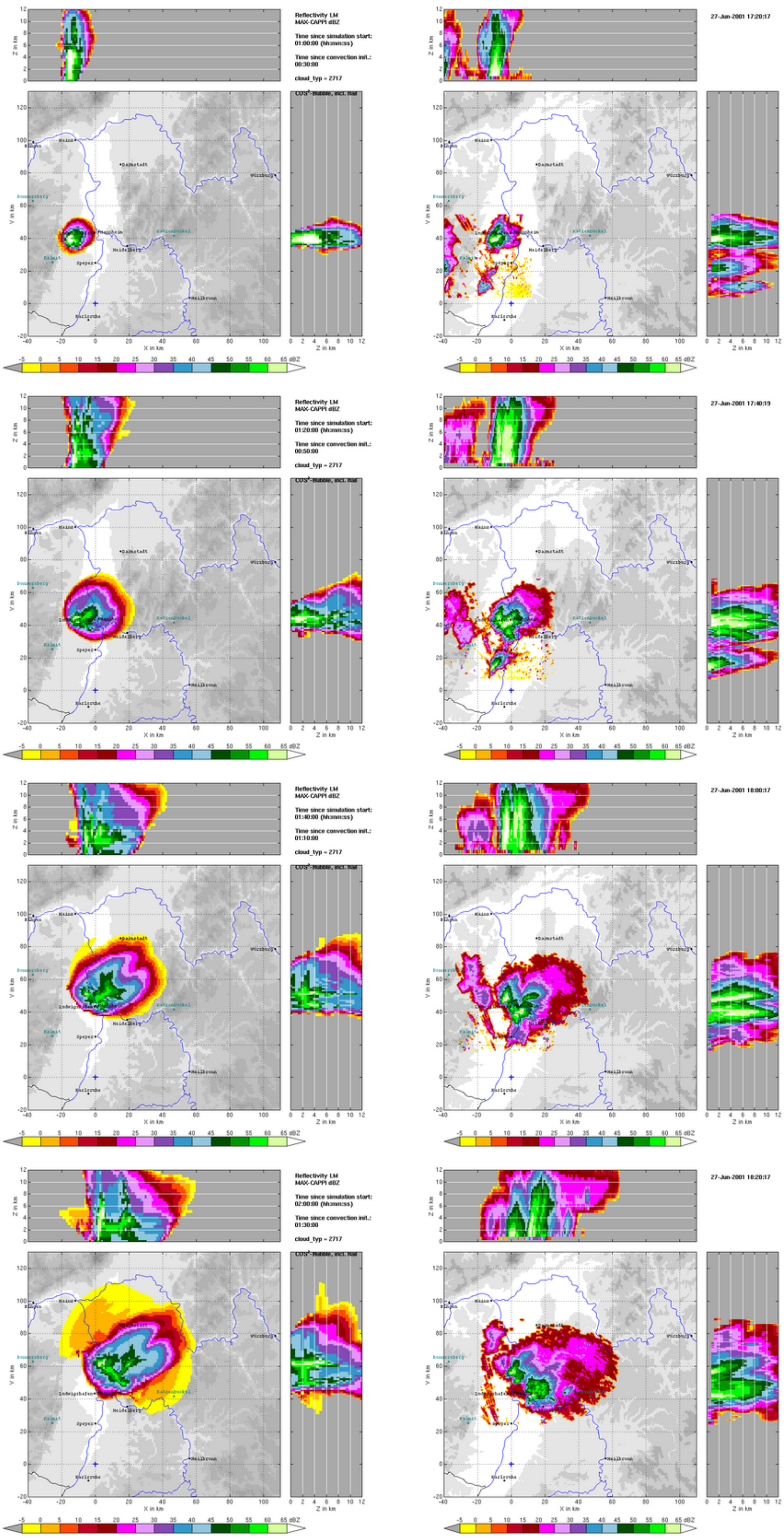

Fig. 2: Series of MAX-CAPPI images of radar reflectivity in dBZ from July 26th 2001, measured by C-band radar (right column) and simulated with the LM (left column). Time increment from one row to the next is 20 min each.

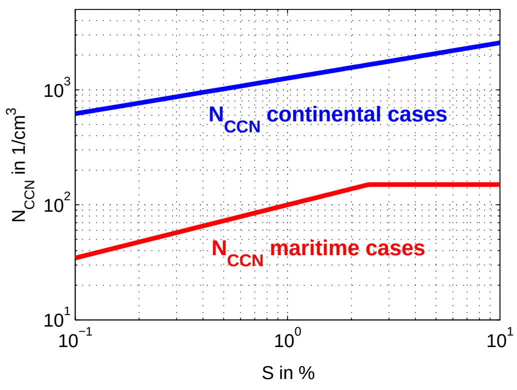

Fig. 3: Number concentration of CCN in cm^{-3} as function of supersaturation in % for the continental and maritime cases considered in this paper.

degree of melting of solid hydrometeors and, on the other hand, an accurate calibration of the radar system would be necessary. Both problems are difficult to deal with.

It is to be mentioned that the additional high-density graupel class denoted FRI-graupel (Noppel et al., 2006) is needed to simulate the observed storm development with reasonable agreement (there are reports on hail observations along the storm track). Maximum simulated vertical velocities do not exceed 42 m s^{-1}, which is reasonable.

From this and other radar comparisons it is concluded that the setup of parameters of the LM and the two-moment bulk microphysical scheme is reasonable to be applicable for our investigations.

4 SENSITIVITY ON TEMPERATURE LEVEL UNDER MARITIME AND CONTINENTAL CCN CONDITIONS

As an example of an interesting sensitivity, results from a small modelling study on the influence of the ambient temperature level (height of the 0°C-isotherm) on convective cell development under different CCN conditions are shown in this section. The ambient temperature level is supposed to have a considerable influence on the cloud microphysical/dynamical feedback, since a colder environment is related to less absolute precipitable water leading to less condensate loading, and the release of latent heat of phase changes occurs at lower heights. Effects are expected to be prominent in cases with low windshear, since then the vorticity dynamics do not entirely control the development.

Four idealized simulations considering a high-$CAPE$- low-windshear-regime were performed, two at a higher ("warm") and two at a lower ("cold") environmental temperature level. For each temperature level, maritime as well as continental CCN conditions were assumed.

In the applied two-moment bulk microphysical parameterization, the treatment of condensation of cloud droplets relies on the classical assumption that the number density of available CCN, N_{CCN}, depends on supersaturation S following powerlaws of the form $N_{CCN} = aS^b$ with parameters a and b (see Seifert and Beheng (2006)). To discern maritime and continental conditions, two different parameter sets of a and b are chosen resulting in the two curves depicted in Fig. 3.

Fig. 4 shows the idealized environmental temperature and dewpoint profiles used as initial- and time-independent boundary conditions for the "warmer" (left panel) and for the "colder" cases (middle panel). The temperature at ground is 28°C in the "warm" cases and 22°C in the "cold" cases, leading to 0-°C-isotherms at heights of 3700 m and 2700 m, resp. These profiles follow those used by Weisman and Klemp (1982) and were constructed in a way that both exhibit the same lifting condensation level (1200 m), level of free convection (1560 m) and level of neutral buoyancy, as well as the same $CAPE$ of approx. 2700 J kg^{-1}, the same vertical buoyancy distribution and the same relative humidity profile above the LCL. The profile of windspeed also follows Weisman and Klemp (1982) (see Fig. 4, right panel) with a maximum value of 5 m s^{-1} in this case, and the wind direction is assumed to be constant with height.

As an alternative to the artificial "warm bubble" approach, convection is triggered in a (probably) more realistic way by leeside wave motion connected with the flow over a single idealized bellshaped mountain (height 2000 m, mountain halfwidth 10 km), which is located upstream of the domain center. The wave flow acts as a quasi-stationary source of initial upward motion, sufficient to initiate convective clouds. Since $CAPE$ is rather large, a multicell system develops by secondary cell triggering and subsequently spreads over the whole domain.

Fig. 5 shows the isosurfaces of mass contents 0.1 g m^{-3} after 3 h for all hydrometeor types considered and for the 4 simulations. The corresponding accumulated precipitation in mm after 3 h can be found in Fig. 6, whereas Fig. 7 presents timeseries of the minimum/maximum vertical velocity W within the model domain in m s^{-1} (left panel), maximum precipitation rate R_{max} at ground in mm/h (middle panel) and total accumulated precipitation P in kg for the 4 simulations. After 3 h, the systems in the "colder" environment are larger and show a more pronounced anvil, and the time series of the minimum/maximum W indicates a faster and more vigorous development compared to the "warm" cases. This behaviour might be explained by the presence of less condensate loading (smaller liquid water drag) and the release of latent heat of freezing at lower heights. However, the maximum precipitation rate is largely dominated by the CCN conditions which affect the rate at which cloud water is converted to rainwater. R_{max} is higher by a factor of 10 in the maritime cases and the onset of precipitation is about 30 min earlier compared to the continental runs. For same CCN conditsions, comparatively small differences in R_{max} are observed for the two temperature levels, indicating that

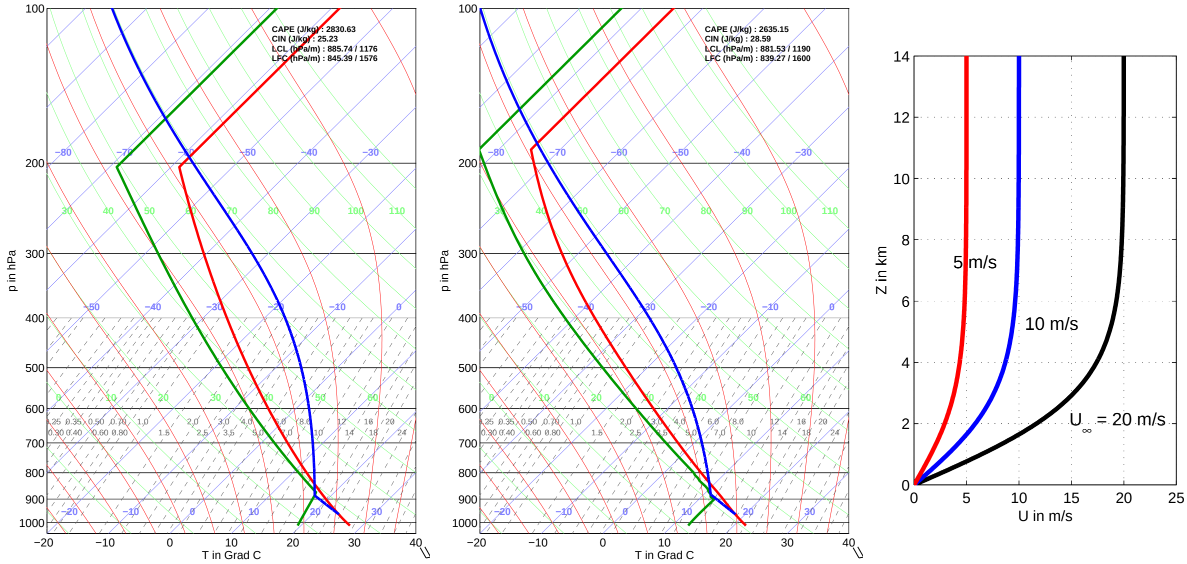

Fig. 4: Idealized thermodynamic conditions, shown as Log-p/Skew-T diagrams for the "cold" cases (left panel) and "warm" cases (middle panel). Idealized wind profiles after Weisman and Klemp (1982) for maximum windspeeds of 5, 10 and 20 $m\,s^{-1}$ (right panel).

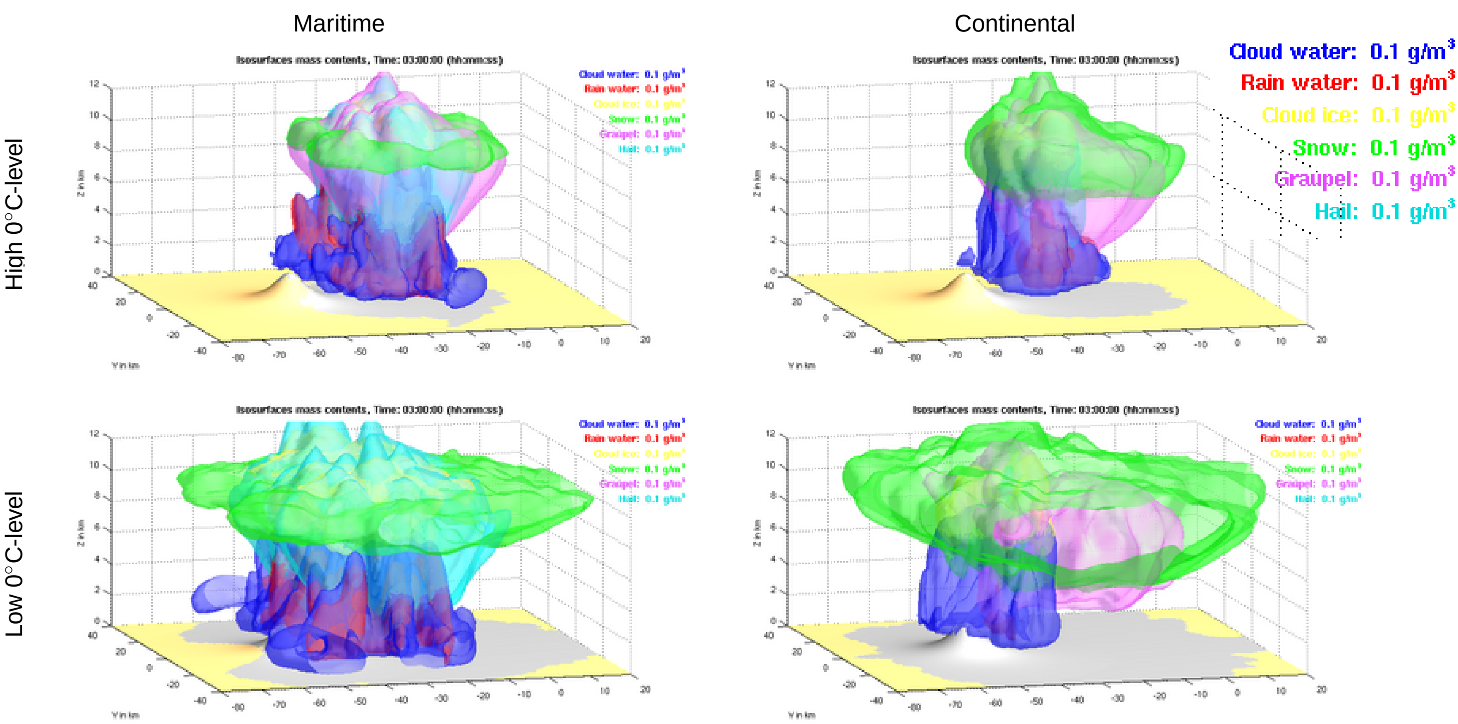

Fig. 5: 3D isosurfaces of the mass content 0.1 $g\,m^{-3}$ for each considered hydrometeor category after 3 h for each of the 4 simulations. Blue = cloud water, red = rain, yellow = ice, green = snow, purple = RIME-graupel, magenta = FRI-graupel. The environmental flow is from left to right. Note the isolated bell-shaped mountain to the left of the figure centers.

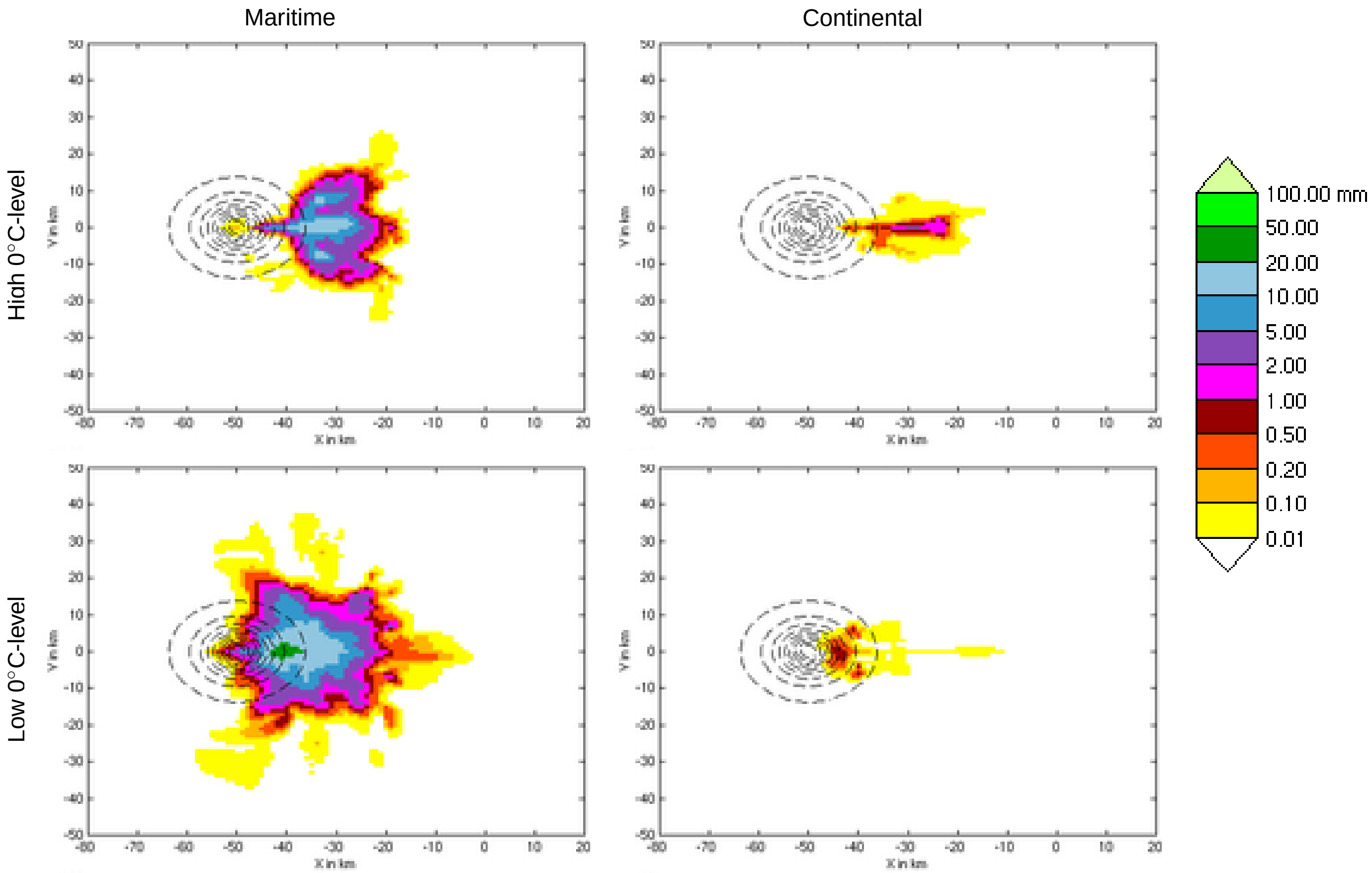

Fig. 6: Plan views of accumulated precipitation at ground in mm after 3 h for each of the 4 simulations.

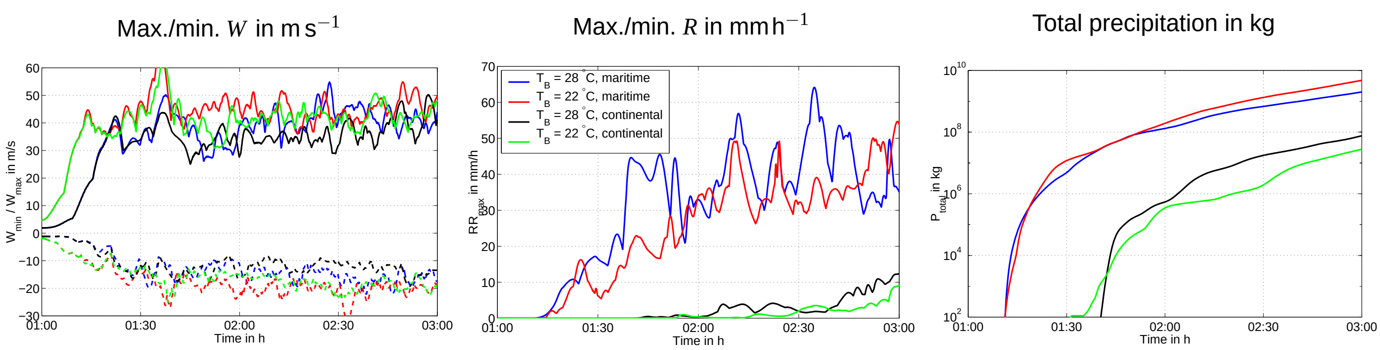

Fig. 7: Timeseries of minimum/maximum vertical velocity in m s^{-1} (left figure), maximum precipitation rate in mm h^{-1} (middle figure), and total accumulated precipitation in kg (right figure) for the 4 simulations.

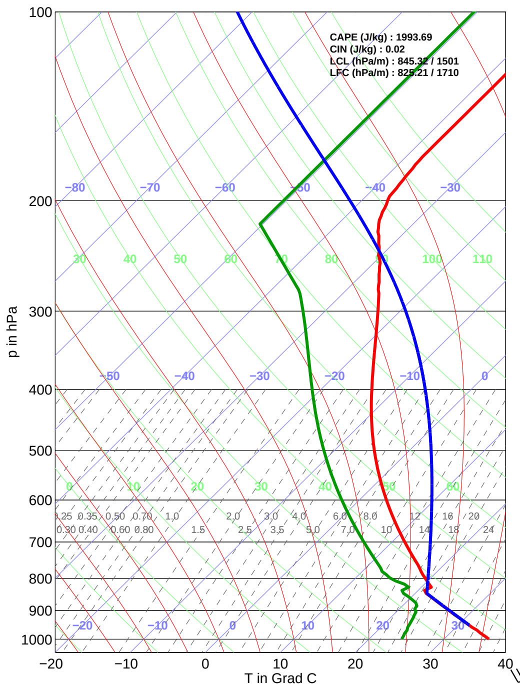

Fig. 8: Idealized thermodynamic conditions for the two simulations with and without 2D mountain ridge, shown as Log-p/Skew-T diagram. Red: ambient temperature, green: ambient dewpoint, blue: pseudoadiabatic lift of an air parcel having the average temperature and humidity of the lowest 100 hPa-layer. Not shown here: wind profile after Weisman and Klemp (1982) (see Fig. 4, right panel) for a maximum windspeed of 20 m s^{-1}.

the effect of absolutely less precipitable water prevailing in the "colder" environment is compensated by a more vigorous development. In total, the rain area and consequently the total accumulated precipitation P at ground is largest for the "cold" maritime case in our simulations (the difference to the "warm" maritime case is about a factor of 2).

5 OROGRAPHIC FLOW AND PREEXISTING DEEP CONVECTIVE SYSTEM

Mountains might affect deep convection not only by providing favorable conditions for triggering convective cells by, e.g., (differential) surface heating on differently oriented slopes, but also through a modification of the ambient environmental conditions caused by mountain wave flow. In this section, the interaction of a preexisting convective system with the flow over an idealized quasi-2D mountain ridge oriented perpendicular to the flow is investigated. The flow over such a mountain ridge exhibits modified temperature- and velocity fields which imply modified profiles of stability and windshear and which in turn might feed back to the convective system. It is supposed that the effect should be most prominent in situations of high windspeed which are usually also connected with long-lived windshear-driven convective systems.

To this end, simulations are performed with the LM using different idealized thermodynamic initial- and boundary conditions, in which a convective system is artificially triggered by a "warm bubble" 60 km upstream the crest of a 2D mountain ridge (height 1000 m, mountain cross-sectional half width 20 km). The initial bubble has a diameter of 20 km in this case. The environmental windspeed follows again the idealized profile shown earlier in Fig. 4 (right panel), now with a maximum value of 20 m s^{-1}. To investigate the effect of the orographic flow on the convective system, these simulations are compared to control runs with flat orography but otherwise same conditions. For the simulations with mountain ridge, convection was initiated only after a spin-up time of 4 h to allow the (dry) mountain wave flow to develop.

An interesting result is found for the temperature and humidity profile depicted in Fig. 8. These conditions comprise a relatively warm environment (temperature at ground 36°C, 0°C-isotherm in 4500 m) with an $CAPE$ of 2000 J kg^{-1} and maximum relative humidity the condensation level of 83 %. Fig. 9 shows 3D isosurfaces of mass content 0.1 g m^{-3} for all considered hydrometeor types (no FRI-graupel in this case) at 40 min after convection triggering (top), 2 h 10 min (middle) and 3 h 10 min (bottom), for the control run (left column) and the simulation with mountain ridge (right column). The accumulated precipitation at the end of the simulation for both runs is presented in Fig. 10, and the timeseries of minimum/maximum W is given in Fig. 11.

In the control run with flat orography, an initially split-cell type convective system further develops into an intense squall-line, moving with the ambient flow from left to right. By contrast, the system dissolves in the simulation with mountain ridge soon after crossing the mountain. In this case, the timeseries of maximum vertical velocity shows a more pronounced minimum at about 1.5 h after convection initiation compared to the control run, following an initial maximum of more than 50 m s^{-1} (which seems unrealistically high and is due to the artificial triggering mechanism). Lateron, this changes to a more pronounced maximum probably connected to triggering of secondary cells before the system dissolves.

So far we do not have a conclusive explanation on the exact mechanisms which lead to the disintegration of the system. However, as a first observation, the system has to pass a zone of increased stability in the vertical column above the mountain crest caused by wave motion: the X-Z-cross section of isentropes and temperature disturbance in Fig. 12 indicates the simulated wave pattern after the spin-up time of 4 h leading to cooling in the lower and warming in the middle troposphere, increasing stability. Further, the leeside mountain flank deflects the cool air outflow connected with rain evaporation below cloud base ("cold pool") downstream (not shown explicitly here). The cold pool now moves slightly ahead of the system, in contrast to

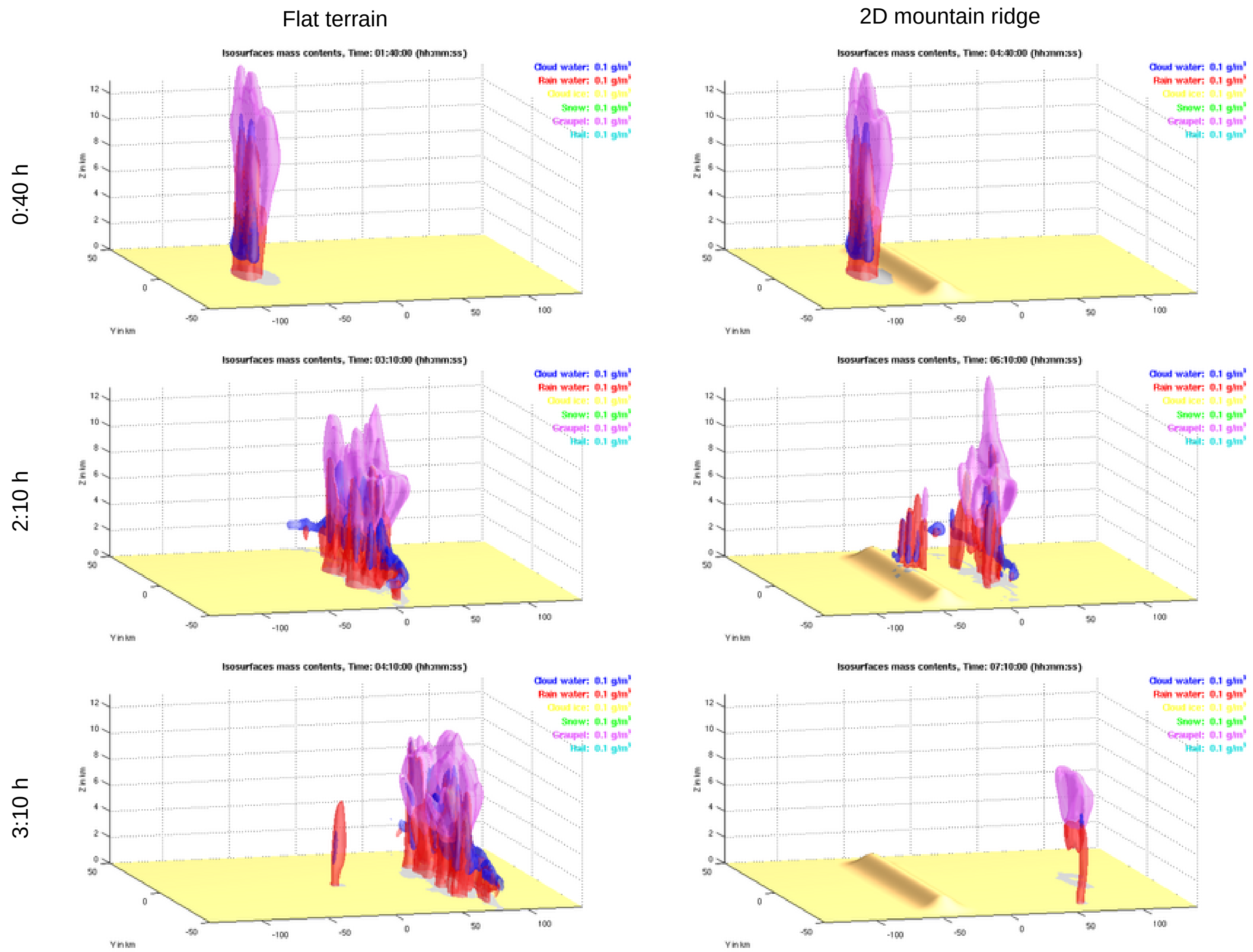

Fig. 9: 3D isosurfaces of mass content 0.1 $g\,cm^{-3}$ for all considered hydrometeor types, similar to Fig. 5. No "hail" (FRI-graupel) considered in this case, original version of the Seifert and Beheng (2006) scheme. Left column: control run without 2D mountain, right column: with mountain. Top row: 40 min after convection triggering, middle row: 2 h 10 min, bottom row: 3 h 10 min.

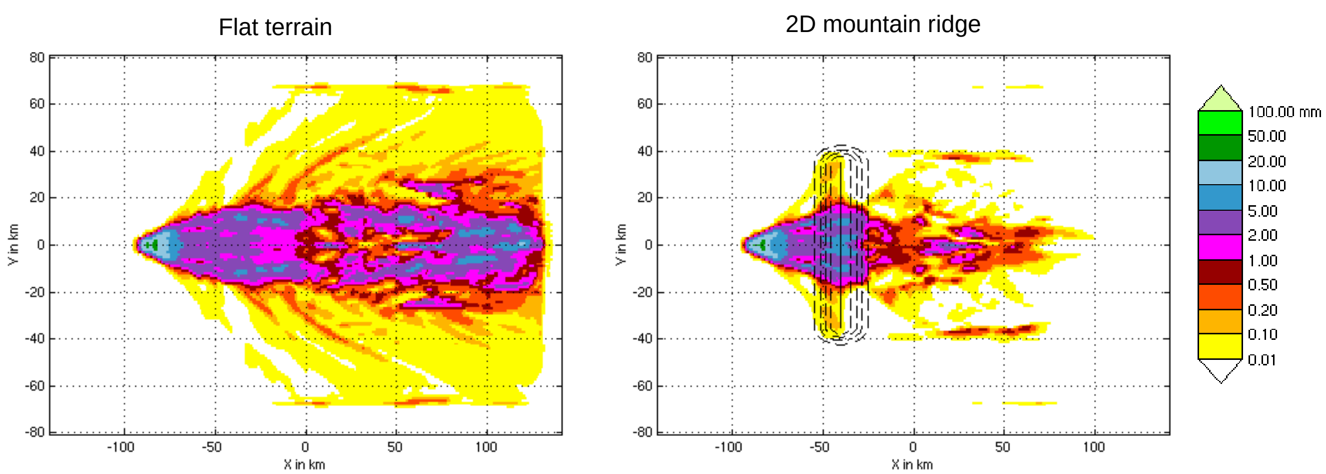

Fig. 10: Plan view of accumulated precipitation in mm 4 h after convection initiation. Control run (left panel) and simulation with 2D mountain ridge (right panel).

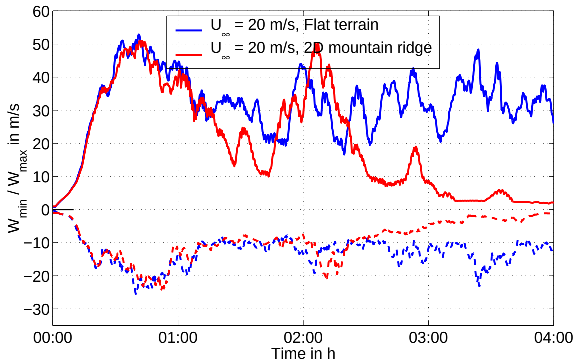

Fig. 11: Minimum/maximum vertical velocity in $m\,s^{-1}$ throughout the model domain for both the control run (blue) and the simulation with mountain ridge (red). The time refers to the initiation of convection.

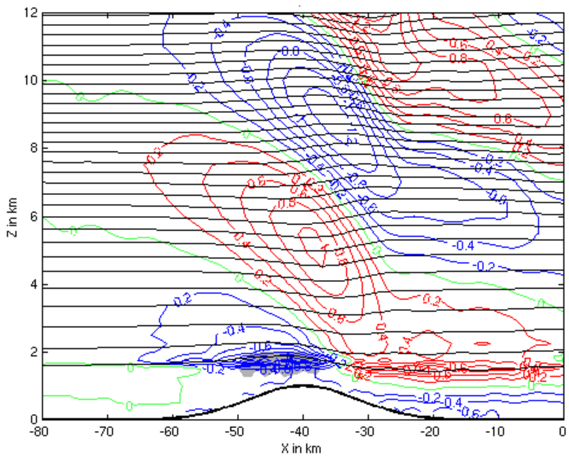

Fig. 12: X-Z-cut at $Y = 0$ after 4 h spin-up time of a) isentropes, spacing of 2 K (black) and b) isolines of temperature disturbance, spacing of 0.2 K (red: positive values, blue: negative values, green: 0-line). The flow is from left to right. An area of liquid water content > 0.001 $g\,m^{-3}$ is shaded grey, indicating a shallow orographic nonprecipitating cloud.

the case with flat orography, enabling a more intense triggering of secondary cells downstream. This might lead to a cut-off of the inflow of the primary system and might favor its disintegration. However, because of the complicated microphysical/dynamical feedback processes it is difficult to investigate which are the exact physical reasons — this remains to be done.

However, other simulations assuming colder environments (with more intense system development) and/ or a higher relative humidity near the LCL do not lead to convection which ceases after having crossed the mountain ridge, whereas in simulations assuming warmer environments and/ or lower LCL humidity, convection dissolves both with and without the mountain. This shows that the flow modification by wave motion is only of minor influence in our simulations and just turns the scale in case the convective system is sufficiently "vulnerable".

6 SUMMARY AND OUTLOOK

This paper shows examples of idealized cloud resolving modeling studies aiming at identifying certain sensitivities of single convective systems to ambient environmental conditions beyond $CAPE$ and windshear. In contrast to other studies, a rather sophisticated two-moment bulk microphysical scheme is used.

To check the performance of the applied model system, observed radar reflectivity fields for cases of single convective systems are compared to reflectivities calculated by accompanying idealized model simulations. An example of these comparisons is presented in Chapter 3, which shows reasonably good agreement within the limitations of both radar measurement and idealized numerical simulation.

In Chapter 4 the height of the 0°C-isotherm is shown to have a considerable influence on cell development in a situation of high instability and low windspeed. The development of a widespread multicell system was more vigorous in a colder environment, which, for the maritime case, leads to about a factor of 2 in total precipitation accumulation.

Chapter 5 presents a study on the interaction of a pre-existing shear-driven and long-lived convective system with the ambient wave flow over a mountain ridge. The system dissolved after having crossed the mountain crest, whereas without the mountain, the system developed into an intense squall-line. However, this effect is presumably of minor importance since it only occured in case the convective system is sufficiently "vulnerable".

There is no "conclusion" given here, since this paper is intended as a report on ongoing work. The described modeling studies act as "precursors" for a more systematic sensitivity study planned for the near future, in which only the most important environmental parameters will be varied over a wider range.

REFERENCES

Doms, G., J. Förstner, E. Heise, H.-J. Herzog, M. Raschendorfer, R. Schrodin, T. Reinhardt and G. Vogel, 2005: *A Description of the Nonhydrostatic Regional Model LM. Part II: Physical Parameterization*, Deutscher Wetterdienst, Offenbach, Germany. Online available: http://www.cosmo-model.org/public/documentation.htm.

Doms, G. and U. Schättler, 2002: *A Description of the Nonhydrostatic Regional Model LM. Part I: Dynamics and Numerics*, Deutscher Wetterdienst, Offenbach, Germany. Online available: http://www.cosmo-model.org/public/documentation.htm.

Noppel, H., U. Blahak, K. D. Beheng and A. Seifert, 2006: A two-moment cloud microphysics scheme with two process-separated modes of graupel, 12. AMS Conference on Cloud Physics, 10. – 14.7.2006, Madison, Wisconsin, **P2.6**.

Seifert, A. and K. D. Beheng, 2006: A two-moment cloud microphysics parameterization for mixed-phase clouds. Part I: Model description, *Meteorol. Atmos. Phys.*, **92**, 45–66.

Seifert, A., A. Khain, A. Pokrovsky and K. D. Beheng, 2006: Aerosol effects on simulated convective storms using spectral (bin) and two-moment bulk mixed-phase cloud microphysics, *Atmos. Res.*, **80**, 46–66.

Weisman, M. L. and J. B. Klemp, 1982: The dependence of numerically simulated convective storms on vertical wind shear and buoyancy, *Mon. Wea. Rev.*, **110**, 504–520.